

# Dynamic modeling and analysis of a 20-cell PEM fuel cell stack considering temperature and two-phase effects

Sang-Kyun Park, Song-Yul Choe\*

*Mechanical Engineering Department, Auburn University, Auburn, AL 36848, USA*

Received 10 December 2007; received in revised form 4 January 2008; accepted 7 January 2008

Available online 21 January 2008

## Abstract

Dynamic characteristics and performance of a PEM fuel cell stack are crucial factors to ensure safe, effective and efficient operation. In particular, water and heat at varying loads are important factors that directly influence the stack performance and reliability. Herein, we present a new dynamic model that considers temperature and two-phase effects and analyze these effects on the characteristics of a stack.

First, a model for a two-cell stack was developed and the simulated results were compared with experimental results. Next, a model for a 20-cell stack was constructed to investigate start-up and transient behavior. Start-up behavior under different conditions where the amplitudes and slopes of a load current, the temperature and flow rate of the coolant, and extra heating of end plates were varied were also analyzed. The transient analyses considered the dynamics of temperature, oxygen and vapor concentration in the gas diffusion media, liquid water saturation, and the variations of water content in the membranes at a multi-step load.

Comparative studies revealed that the two-phase effect of water predominantly reduces oxygen concentration in the catalysts and subsequently increases the activation over-potential, while temperature gradients in the cells directly affect the ohmic over-potential. The results showed that the heat-up time at start-up to achieve a given reference working temperature was inversely proportional to the amplitude of the current density applied and the flow rate and temperature of the coolants. In addition, the asymmetric profile of the stack temperature in the stack was balanced when the temperature of the coolant supplied was reheated and elevated. Analyses of transient behaviors for a 20-cell stack showed that strong temperature gradients formed in the last four end cells, while temperature, oxygen concentration, vapor concentration, liquid water saturation, and membrane water content in the rest of the cells were uniform.

© 2008 Elsevier B.V. All rights reserved.

*Keywords:* PEMFC; Stack; Temperature; Two-phase water; Dynamics

## 1. Introduction

Polymer electrolyte membrane fuel cells (PEMFC) are the best candidates for an efficient power source to supply our power needs in the future. This is particularly true because of their low operating temperature, relatively short start-up time, high power density, and efficiency. In addition, the PEM fuel cell produces zero emissions because the chemical reaction of hydrogen and oxygen ejects pure water. These advantages are superior to those of internal combustion engines and PEMFC hold promise

for a variety of applications in vehicles, utilities, and portable electronics.

The life span required for the fuel cell stack is roughly 3000–5000 h for passenger cars, up to 20,000 h for commercial vehicles, and up to 40,000 h for stationary applications. The durability required depends upon operating conditions at start-up, normal operation, and shutdown. Particularly, heat and water management determine the durability of the catalysts. For example, improper operating conditions such as low reactant flows, high and low humidity, or high and low temperature can accelerate Pt particle growth size and dissolve the particles from the carbon support [1–4]. As a result, the electro catalyst surface area decreases and the overall performance drops because of the growth in platinum particle size. Not only a low humidity but also an elevated temperature contributes to particle growth [2,3]. It should be emphasized that water and heat in an oper-

\* Corresponding author at: Mechanical Engineering Department, Auburn University, 201 Ross Hall, Auburn, AL 36848, USA. Tel.: +1 344 844 3382; fax: +1 334 844 3307.

*E-mail addresses:* [parksan@auburn.edu](mailto:parksan@auburn.edu) (S.-K. Park), [choe@eng.auburn.edu](mailto:choe@eng.auburn.edu) (S.-Y. Choe).

**Nomenclature**

$a$	water activity
$A$	area ( $\text{m}^2$ )
$b$	parametric coefficient (V)
$c$	concentration of species ( $\text{mol cm}^{-3}$ )
$C$	mass concentration ( $\text{kg m}^{-3}$ )
$C_p$	specific heat capacity ( $\text{J kg}^{-1} \text{K}^{-1}$ )
$D_m$	diffusion coefficient ( $\text{m}^2 \text{s}^{-1}$ )
$\langle D_m \rangle$	effective diffusivity ( $\text{m}^2 \text{s}^{-1}$ )
$D_{\text{water}}$	water diffusion coefficient
$E$	open circuit potential (V)
$i$	current density ( $\text{A m}^{-2}$ )
$I$	current (A)
$m$	mass (kg) or $\text{O}_2$ of vapor
$M$	molecular mass ( $\text{kg mol}^{-1}$ )
$n$	number of electrons (2 or 4)
$n_d$	electro-osmotic drag coefficient
$p$	pressure (atm)
$\dot{Q}$	heat transfer ratio (W)
$R_{\text{ele}}$	electrical resistance ( $\Omega$ )
$s$	liquid water saturation ratio
$\Delta S$	change in entropy ( $\text{J mol}^{-1} \text{K}^{-1}$ )
$t$	thickness (cm or m), time (s)
$T$	temperature (K)
$V$	volume ( $\text{m}^3$ ) or voltage (V)
$W$	mass flow ( $\text{kg s}^{-1}$ )

*Greek letters*

$\varepsilon$	porosity
$\xi$	constant parametric coefficient
$\eta$	over-potential (V)
$\lambda$	water content
$\rho$	mass density ( $\text{kg m}^{-3}$ )
$\sigma_{\text{mem}}$	membrane conductivity ( $\Omega^{-1} \text{cm}^{-1}$ )

*Subscripts*

an	anode
ca	cathode
$i$	cell number
in	inlet
$j$	layer
k	reactant or product gases
l	anode or cathode
mem	membrane
sat	saturation
sou	source
v	vapor

ating stack are the key factors that determine reliability and durability.

To date, most of the internal variables in an operating stack are inaccessible and hard to measure because the cells are composed of thin layers and fully sealed. Moreover, the interrelated variables in an operating cell as well as a stack make it difficult for

the design and system engineers to understand the mechanism and to optimally design the stack. Therefore, simulations have become more accepted methods for studying the stack behavior. This requires computer models that describe the real behaviors of the fuel cell stack.

Currently, models for the PEM fuel cell [5–10] can be categorized into multi-dimensional and one-dimensional models. The multi-dimensional model solves governing equations by using Computational Fluid Dynamics and provides a high resolution of flow characteristics of reactants, fuel, byproducts, and transport of charges. This is particularly advantageous and useful for analysis of a single cell, but is limited for a stack because of the enormous computational time and the associated parameters and variables required for the models. Moreover, it is impossible to integrate system components into a stack model. Thus, these models are usually applied to investigate parts of complex domains such as flow fields of a single cell and to predict the performance of a single cell.

By contrast, the one-dimensional model or quasi-one-dimensional model is a macroscopic model that describes layers in a cell. These simplified models do not provide detailed analytical mechanisms of a cell, but allow representations of the dynamic behavior of a multi-cell stack and analysis of the interactions between the stack and system components. Therefore, these models are preferred for investigating the dynamics of the system.

Many authors have proposed such models. Springer et al. [10] proposed a model capable of analyzing water transport in the membrane and the performance of a cell even though it was isothermal and one-dimensional. Nguyen and White [11] developed a model used for analysis of the effects of humidification and temperature on cell performance. Amphlett et al. [12] proposed empirical equations representing  $I$ – $V$  characteristics of a cell at different working temperatures. However, none of the models were able to represent the dynamics of the physical properties inside the cell at a varying load. Pukrushpan et al. [13] proposed a model that considered the dependence of the proton conductivity on the water concentration and temperature. However, the water concentration of the membrane obtained from the relative humidity (RH) was calculated from an average of the anode and cathode RH. In fact, the amount of water in the membrane is larger than that residing in the anode and cathode side. Thus, the RH in the anode and cathode varied rapidly, while the RH in the membrane varied slowly [14]. In addition, the oxygen concentration in the gas diffusion layer (GDL) on the cathode side was continuously changing in operating environments and significantly affected the performance of the cell. Pathapati et al. [15] added a double layer capacitance that was thought to represent the effects of charges. However, both models assumed that the behavior of a stack was the cell number times the single cell performance and that the working temperature in a stack was constant.

A one-dimensional thermal model developed by Khandelwal et al. [16] was used to predict the temperature distribution at a cold start. However, the model did not provide transient analysis of temperature at a varying load. Explicit thermal dynamic models with the coolant channel coupled with a 1D cell model were proposed by Amphlett et al. [17], Wöhr et al. [18], and Wetton

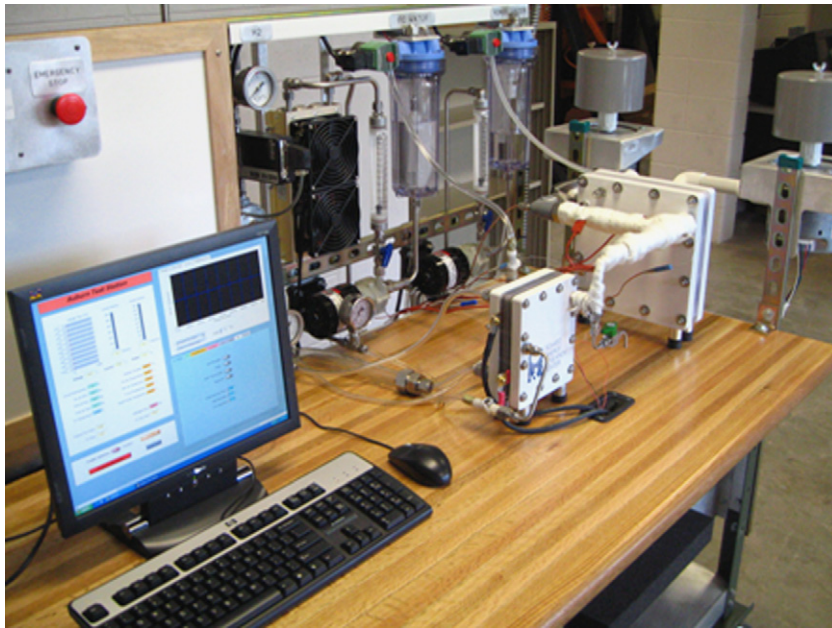


Fig. 1. Experimental apparatus.

et al. [19]. In addition, Sundaresan and Moore [20] significantly complemented dynamics using simplified thermodynamic models to analyze the performance of the stack. The model was based on layers and facilitated analysis of start-up behavior from a sub-freezing temperature. Effects of a varying load on dynamics of temperature were also investigated by Shan and Choe [21,22]. However, all of the above proposed models assumed that water in the stack was vapor or ignored transient behavior. McKay et al. [23] developed a simple two-phase model for a gas diffusion layer and used it to represent the effects of liquid water and vapor on the performance of the cells. del Real et al. [24] presented a two-phase dynamic model. However, neither of these models considered the dynamic variation of temperature and its effects on the performance of a stack and water balance in the membrane.

The model we developed is effective and useful for describing dynamics at varying loads and includes the following major improvements over other models: (1) temperature distribution in the through-plane of a cell and its effects on the characteristics of the membrane, catalysts, gas diffusion layers, and gas flow channels; (2) the dynamic water balance in the membranes; (3) the two-phase effects in gas diffusion layers and gas channels; and (4) a coupled 20-cell stack. This analysis included comparisons between a single-phase and a two-phase model, start-up behavior of a 20-cell stack, and the transient behavior at a step load. Temperature distribution and the change of overpotentials along with the associated cell voltages were the major parameters investigated.

## 2. Test equipment

The experimental apparatus is shown in Fig. 1. The test equipment was devised to test a PEM fuel cell system that consists of a two-cell stack and the balance-of-the-plant that includes an air

supply, a humidifier, a hydrogen delivery system, a coolant circuit, controls, and an E-load. A commercial software package, LabVIEW, is used to correct and process the data. The stack was constructed with two cells separated by a thermally conductive plate in order to minimize the potential influence of the coolants on the working temperature. Other components used in the cells are the same as those in a typical assembly. The cell fabricated had an active area of  $140 \text{ cm}^2$ . The maximum electric power of the stack was 80 W.

## 3. Dynamic stack model

### 3.1. Model description

The model was developed on the basis of layers in a unit cell that consist of a membrane-electrode-assembly (MEA), two catalyst layers, two gas diffusion layers, and two gas channels sandwiched between coolant channels as shown in Fig. 2. The input variables for the model were current load, mass flow rate, the gas components fraction, temperature, pressure, and relative humidity of reactants as well as the temperature and flow rate of coolants at the inlets.

The main assumptions used to develop the model are as follows:

- Reactants are ideal gases.
- There is no pressure gradient between the anode and cathode side (gas is transported by diffusion, not convection).
- There is no gas pressure drop between the inlet and the outlet of the gas channel.
- The temperature gradient is linear across the layers in a fuel cell.
- The thermal conductivity for the materials in a fuel cell is constant.

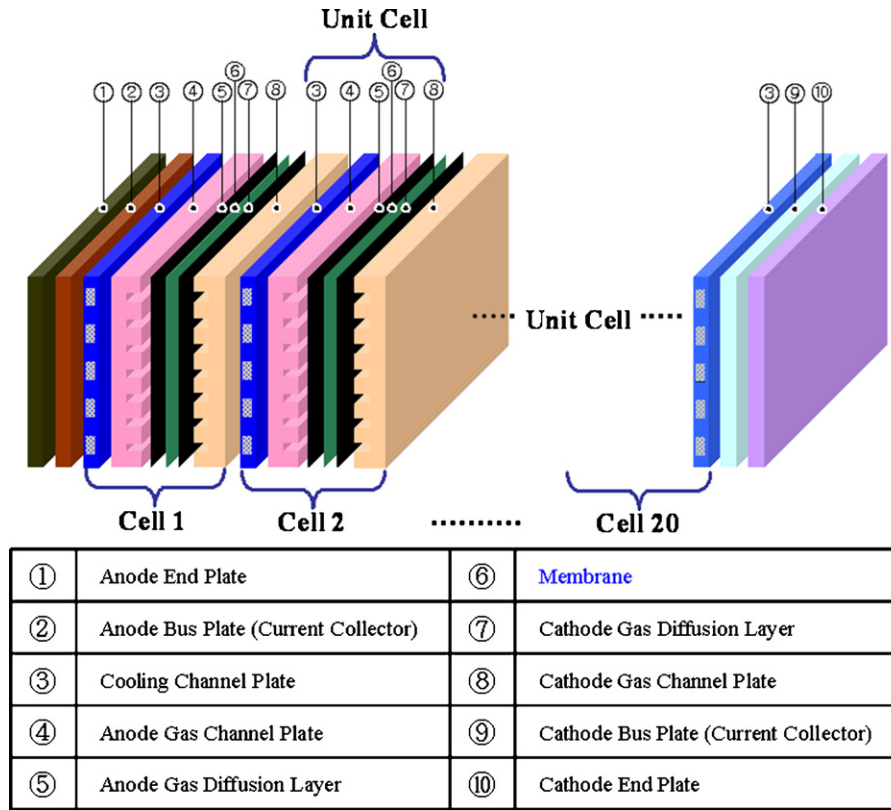


Fig. 2. Schematic simulation domain for a 20-cell stack.

- Anodic over-potential is negligible.
- There is no current density gradient across the cathode catalyst layer (the reaction is complete at the cathode catalyst layer surface).
- Latent heat during a phase transition is not considered.

Based on these assumptions, we developed the models described in the following sections. Static behaviors of a cell model are based on voltage equations and the effects of temperature distribution in a cell, water balance in the membrane, and gas dynamics in the cathode gas diffusion layer with a two-phase phenomenon are described below. A cell is constructed by the connection of individual models for layers as shown in Fig. 2.

### 3.2. Governing equations

A model for a single cell and stack was developed and the composition of the individual layers and the performance were analyzed in detail [21,22]. Table 1 summarizes the parameters of the stack components.

#### 3.2.1. I–V characteristic

The I–V characteristic is given by the difference between the open circuit voltage  $E_i$ , and the over-potentials that include the activation over-potential in the catalyst on the cathode side  $\eta_{i,act}$ , and the ohmic over-potential in the membrane  $\eta_{i,ohm}$ , and the concentration over-potential  $\eta_{i,con}$ .

$$V_i = E_i - \eta_{i,act} - \eta_{i,ohm} - \eta_{i,con} \quad (1)$$

Table 1  
Parameters used for models

	Thickness (m)	Thermal conductivity ( $\text{W m}^{-1} \text{K}^{-1}$ )	Density ( $\text{kg m}^{-3}$ )	Specific heat ( $\text{J kg}^{-1} \text{K}^{-1}$ )
End plate	0.028575	0.228	1800	1416
Coolant plate	0.001524	95	1780	935
Gas channel plate	0.001524	105	1820	935
Diffusion media	0.0004064	65	840	558
Catalyst layer	0.0000035	0.2	770	387
Membrane	0.000035	0.21	1967	1100
Active area ( $\text{cm}^2$ )	140			

The open circuit potential  $E_i$  is derived from the energy balance between chemical and electrical energy [12]:

$$E_i = 1.229 - 0.85 \times 10^{-3}(T_i - 298.15) + 4.3085 \times 10^{-5} T_i \left[ \ln(p_{i,H_2}) + \frac{1}{2} \ln(p_{i,O_2}) \right] \quad (2)$$

The activation over-potential,  $\eta_{i,act}$  is expressed as a function of the working temperature and the oxygen concentration [12,28,29]:

$$\eta_{i,act} = \xi_1 + \xi_2 T_i + \xi_3 T_i \ln(c_{i,O_2}) + \xi_4 T_i \ln(I) \quad (3)$$

where  $\xi$  represents constant parametric coefficients,  $I$  is current (A), and  $c_{O_2}$  is concentration of oxygen in the catalyst interface of the cathode ( $\text{mol cm}^{-3}$ ) (Table 2).

Table 2  
Electrochemical parameters [12,28,29]

Parameters	Value
$\xi_1$	-0.934
$\xi_2$	0.00342
$\xi_3$	0.00008
$\xi_4$	-0.00019
$b$	0.05
$i_{\max}$	1.5

The ohmic over-potential  $\eta_{i,\text{ohm}}$  is obtained from Ohm's law [10,11]:

$$\eta_{i,\text{ohm}} = i R_{i,\text{ohm}} = \frac{i t_{\text{mem}}}{\sigma_{i,\text{mem}}} \quad (4)$$

where  $i$  is the actual current density ( $\text{A cm}^{-2}$ ), and  $R_{\text{ohm}}$ ,  $t_{\text{mem}}$  and  $\sigma_{\text{mem}}$  denote ohmic resistance ( $\Omega \text{cm}^2$ ), membrane thickness (cm) and conductivity ( $1 \Omega^{-1} \text{cm}^{-1}$ ), respectively. The membrane conductivity is given as a function of the working temperature [10,11]:

$$\sigma_{i,\text{mem}} = \sigma \exp \left[ 1268 \left( \frac{1}{303} - \frac{1}{T_i} \right) \right] \quad (5)$$

$$\sigma = 0.005139 \lambda_{i,\text{mem}} - 0.00326$$

where  $\lambda_{i,\text{mem}}$  is the membrane water content.

The concentration over-potentials,  $\eta_{i,\text{con}}$  are approximated by the following equation [28,29]:

$$\eta_{i,\text{con}} = -b \ln \left( 1 - \frac{i}{i_{\max}} \right) \quad (6)$$

where  $b$  is a parametric coefficient (V) that was derived from the single cell characteristic and assumed to be identical for all of the cells in the stack,  $i$  and  $i_{\max}$  denote the actual and the maximum current density ( $\text{A cm}^{-2}$ ).

Finally, the stack voltage is the sum of all of the individual cell voltages.

$$V_{\text{stack}} = \sum_i V_{i,\text{cell}} \quad (7)$$

### 3.2.2. Energy balance

If a cell is assembled with cubical layers in which thermo-physical properties are isotropic and constant, the total energy changes in a controlled volume equal the sum of the energy exchange at boundaries and internal energy resources according to the energy conservation equation. In fact, the energy exchanges at boundaries occur in three ways: (a) mass flow into each volume; (b) conduction across the cell; and (c) convection occurring between bipolar plates with the coolant, the reactants and water. Thus, the thermal-dynamic behavior can be described with the following energy conservation equation [22]:

$$\sum_j m_j C_{p,j} \frac{dT_j}{dt} = \underbrace{\sum_k m_k C_{p,k} (T_{\text{in}} - T_j)}_{\text{mass flow in}} + \dot{Q}_{\text{convection}} + \dot{Q}_{\text{conduction}} + \dot{Q}_{\text{sou}} \quad (8)$$

Hence, the internal energy source is mainly composed of the entropy loss and the chemical energy required for oxygen and protons to overcome the barrier of the over-potentials in both catalyst layers. In addition, other heat sources are associated with ohmic losses by transport of electrons and protons in a cell.

$$\dot{Q}_{\text{sou}} = i A \left( -\frac{T_i \Delta S}{nF} + \eta_i + i A R_{\text{ele}} \right) \quad (9)$$

where the entropy change is  $\Delta S = 0.104 \text{ J mol}^{-1} \text{ K}^{-1}$  for the anode, and  $\Delta S = -323.36 \text{ J mol}^{-1} \text{ K}^{-1}$  for the cathode [16,27].

### 3.2.3. Water balance in the membrane

Water content in the membrane determines the proton conductivity. The dynamics of the water content is described by two effects, the electro-osmotic driving forces because of the electrochemical potential difference between the cathode and anode, and the diffusion caused by the water concentration gradient at the two boundaries. Considering the water mass flows at the boundaries of the membrane layer, the dynamics of the water concentration in the membrane was described as follows [10,21]:

$$\lambda_{i,\text{mem}} = \frac{C_{i,\text{H}_2\text{O},\text{mass}}/M_{\text{H}_2\text{O}}}{\frac{\rho_{\text{dry},\text{mem}}}{M_{\text{mem}}} - 0.0126 C_{i,\text{H}_2\text{O},\text{mass}}/M_{\text{H}_2\text{O}}} \quad (10)$$

$$\dot{m}_{i,\text{mem}} = \frac{d(C_{i,\text{H}_2\text{O},\text{mass}} A t_{\text{mem}})}{dt} =$$

$$W_{i,\text{ele},\text{mem},\text{an}} - W_{i,\text{ele},\text{mem},\text{ca}} + W_{i,\text{diff},\text{mem},\text{an}} + W_{i,\text{diff},\text{mem},\text{ca}}$$

where  $C$  is the mass concentration ( $\text{kg m}^{-3}$ ),  $M$  is the mole mass ( $\text{kg mol}^{-1}$ ),  $\rho$  is the membrane dry density and  $A$  is the fuel cell area ( $\text{m}^2$ ).

The electro-osmotic driving force exerted by two different electrochemical potentials at the anode and cathode determines the water mass flows of  $W_{i,\text{ele},\text{mem},\text{an}}$  and  $W_{i,\text{ele},\text{mem},\text{ca}}$  at the boundaries of the membrane layer. In addition, the diffusion caused by the water concentration gradient at the two boundaries makes up the mass flows of  $W_{i,\text{diff},\text{mem},\text{an}}$  and  $W_{i,\text{diff},\text{mem},\text{ca}}$ . Those relationships are described by Eqs. (11) and (12) [9,10].

$$W_{i,\text{ele},\text{mem},1} = M_{\text{water}} A n_{d,i,1} \frac{i}{F} \quad (11)$$

$$W_{i,\text{diff},\text{mem},1} = M_{\text{water}} A D_{\text{water},i,1} \frac{(C_{i,1} - C_{i,\text{mid}})}{t_{\text{mem}}} \quad (12)$$

where the electro-osmotic drag coefficient  $n_{d,i,1}$ , the water concentration  $C_{i,1}$  and the water diffusion coefficient  $D_{\text{water},i,j}$  are calculated from the empirical equations [10].

$$n_{d,i,1} = 0.0029 \lambda_{i,1}^2 + 0.05 \lambda_{i,1} - 3.4 \times 10^{-19} \quad (13)$$

$$C_{i,1} = \frac{\rho_{\text{dry},\text{mem}}}{M_{\text{mem}}} \lambda_{i,1}, \quad C_{i,\text{mid}} = \frac{\rho_{\text{dry},\text{mem}}}{M_{\text{mem}}} \lambda_{i,\text{mem}} \quad (14)$$

$$D_{\text{water},i,1} = D_{\lambda,i,1} \exp \left( 2416 \left( \frac{1}{303} - \frac{1}{T_{\text{mem},i}} \right) \right) \quad (15)$$

$$D_{\lambda,i,1} = \begin{cases} 10^{-6} & 2 > \lambda_{i,1} \\ 10^{-6}(1 + 2(\lambda_{i,1} - 3)) & 3 \geq \lambda_{i,1} \geq 2 \\ 10^{-6}(3 - 1.67(\lambda_{i,1} - 3)) & 4.5 > \lambda_{i,1} > 3 \\ 1.25 \times 10^{-6} & \lambda_{i,1} \geq 4.5 \end{cases} \quad (16)$$

The boundary water content  $\lambda_{i,1}$  is a function of water activity  $a_{i,1}$ , which is calculated from the water vapor partial pressure:

$$\lambda_{i,1} = \begin{cases} 0.043 + 17.81a_{i,1} - 39.85a_{i,1}^2 + 36a_{i,1}^3 & 1 \geq a_{i,1} > 0 \\ 14 + 1.4(a_{i,1} - 1) & 3 \geq a_{i,1} > 1 \\ 16.8 & a_{i,1} \geq 3 \end{cases} \quad (17)$$

$$a_{i,1} = \frac{P_{v,i,1}}{P_{\text{sat},i,1}} \quad (18)$$

### 3.2.4. Gas diffusion layer with a two-phase effect

The phase of water in the GDL plays a significant role in transport of water and reactants. The model for the GDL considers the mass transport in a gas and liquid phase and the phase transition between liquid water and water vapor. Most dynamic models proposed for the GDL assumed that water generated and supplied were water vapor, so that the effects of liquid water was generally neglected. However, when liquid water is involved, diffusion characteristics are different from those in the vapor state. The diffusion in the GDL can be redefined by introducing an effective diffusivity that describes the diffusion behavior of vapor and liquid water in a capillary [23,25]. Porosity is reflected in the equation, while no tortuosity was considered.

$$\langle D_m(k) \rangle = D_m \varepsilon \left( \frac{\varepsilon - 0.11}{1 - 0.11} \right)^{0.785} (1 - s(k))^2 \quad (19)$$

$$\varepsilon = \frac{V_{\text{pore}}}{V_{\text{GDL}}}, \quad s(k) = \frac{V_{\text{liquid}}(k)}{V_{\text{pore}}}$$

$m = \text{O}_2, \text{ vapor}$

where  $\langle D_m \rangle$  is the effective diffusivity ( $\text{m}^2 \text{s}^{-1}$ ),  $D_m$  is the diffusion coefficient ( $\text{m}^2 \text{s}^{-1}$ ) at a single phase,  $\varepsilon$  is the porosity of the diffusion layer,  $s$  is the liquid water saturation ratio,  $V_{\text{pore}}$  is the pore volume of the GDL ( $\text{m}^3$ ),  $k$  is the number of each domain in the GDL,  $V_{\text{GDL}}$  is the total volume of the GDL ( $\text{m}^3$ ), and  $V_{\text{liquid}}$  is the volume of the liquid water ( $\text{m}^3$ ).

The simulation domain for half a cell is depicted in Fig. 3, where the GDL was divided into three sub-domains in order to calculate gradients of species. The points of 0 and 4 are the boundary conditions, while 1, 2 and 3 are the middle points of the sub-domains.

The water vapor produced,  $N_{v,0}$ , and the oxygen consumed,  $N_{O_2,0}$ , were expressed as a function of a current. The total molar flux of the water vapor at the boundary was given as follows:

$$N_{v,0} = \frac{I}{2F}, \quad N_{O_2,0} = \frac{I}{4F} \quad (20)$$

$$N_{v,\text{catalyst}} = N_{v,0} + N_{v,\text{mem}}$$

where  $N_{v,\text{mem}}$  is defined in the Eq. (10).

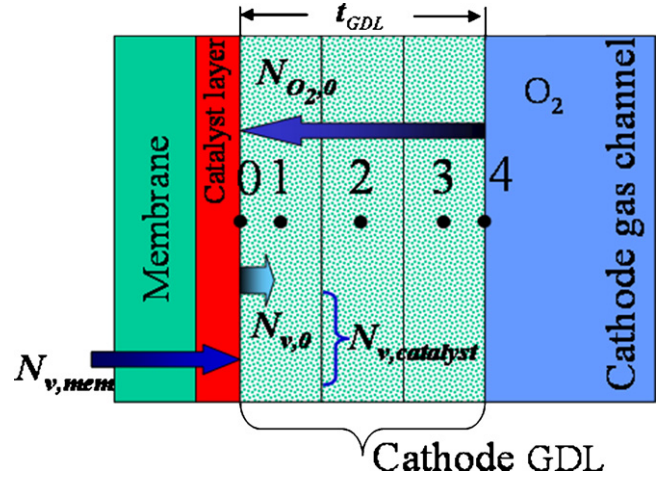


Fig. 3. Schematic simulation domain for the GDL with a two-phase phenomenon.

The molar flux is expressed as a function of the effective diffusivity and the gas concentration gradient, where  $z_{\text{ca}}(k)$  represents the ratio of the species molar flux:

$$z_{\text{ca}}(k) = \begin{cases} N_{v,0}/N_{O_2,0} & \text{for } k = 1 \\ N_v(k-1)/N_{O_2}(k-1) & \text{for } k = 2, 3 \end{cases}$$

$$N_{O_2}(k) = \frac{-\langle D_{O_2}(k) \rangle}{1 - x_{O_2}(k)(1 + z_{\text{ca}}(k))} \frac{c_{O_2}(k+1) - c_{O_2}(k)}{y t_{\text{GDL}}} \quad (21)$$

$$N_v(k) = \frac{-\langle D_v(k) \rangle}{1 - x_v(k)(1 + 1/z_{\text{ca}}(k))} \frac{c_v(k+1) - c_v(k)}{y t_{\text{GDL}}}$$

$N$  is the molar flux ( $\text{mol s}^{-1} \text{m}^{-2}$ ),  $x$  is the molar ratio of the species, and  $y$  is the coefficient dependent upon the number of the sub-domain.

The time derivatives of the gas concentrations are a function of the ratio of the species molar flux [23]:

$$\frac{dc_{O_2}}{dt}(k) = -\frac{N_{O_2}(k) - N_{O_2}(k-1)}{y t_{\text{GDL}}} \quad (22)$$

$$\frac{dc_v}{dt}(k) = -\frac{N_v(k) - N_v(k-1)}{y t_{\text{GDL}}} + R_{\text{evap}}(k)$$

Hence, the evaporation rate is determined by the difference between the saturation and vapor pressure [23,25]:

$$R_{\text{evap}}(k) = \gamma \frac{p_{v,\text{sat}}(T) - p_v(k)}{RT} \quad (23)$$

where  $\gamma$  is the volumetric condensation coefficient ( $\text{s}^{-1}$ ),  $p$  is pressure (Pa) and  $R$  is the ideal gas constant ( $\text{J mol}^{-1} \text{K}^{-1}$ ).

According to the mass balance, the rate of the liquid water volume at each of the points was obtained as follows:

$$\frac{dV_{\text{liquid}}}{dt}(k) = \begin{cases} \frac{-M_v \varepsilon V_{\text{GDL}} R_{\text{evap}}(k) - W_{\text{liquid}}(k)}{\rho_{\text{liquid}}}, & k = 1 \\ \frac{-M_v \varepsilon V_{\text{GDL}} R_{\text{evap}}(k) + W_{\text{liquid}}(k-1) - W_{\text{liquid}}(k)}{\rho_{\text{liquid}}}, & k = 2, 3 \end{cases} \quad (24)$$

The mass flow of the liquid water in the Eq. (24),  $W_{\text{liquid}}$ , was derived from the pressure gradient driven flow in a

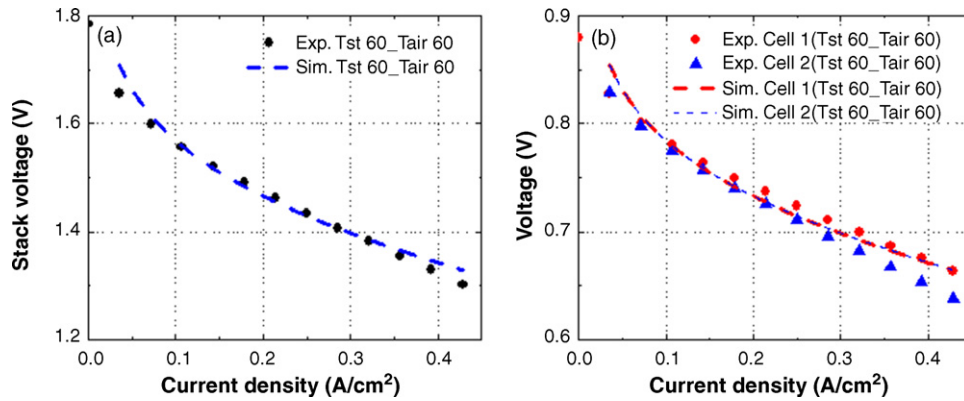


Fig. 4. Comparison of the simulated and experimental stack and cell voltages at a two-cell stack.

capillary [23,25]:

$$W_{\text{liquid}}(k) = -\frac{A\rho_{\text{liquid}}K K_{\text{rl}}}{\mu_{\text{liquid}}} \left| \frac{dp_c}{dS} \right| \frac{S(k+1) - S(k)}{y_{\text{GDL}}},$$

$$S(k) = \begin{cases} \frac{s(k) - s_{\text{im}}}{1 - s_{\text{im}}}, & s_{\text{im}} < s(k) \leq 1 \\ 0, & 0 \leq s(k) \leq s_{\text{im}} \end{cases} \quad (25)$$

where  $\rho$  is the liquid water density ( $\text{kg m}^{-3}$ ),  $K$  is the absolute permeability ( $\text{m}^2$ ),  $K_{\text{rl}}$  is the relative permeability of liquid water that was assumed to be equal to  $S^3$ ,  $\mu$  is the viscosity of water ( $\text{kg m}^{-1} \text{s}^{-1}$ ),  $|dp_c/dS|$  is the slope of capillary pressure (Pa),  $S$  is the reduced liquid water saturation and  $s_{\text{im}}$  is the immobile saturation.

Table 3 summarizes the parameters of the GDL used for the simulation. The range of the simulated liquid water saturation shown in Fig. 10 was 0.12–0.18, which is comparable with those in Ref. [25].

#### 4. Results and discussion

Simulations to analyze dynamic performance of a stack were performed. First,  $I$ – $V$  characteristics of the stack as well as the individual cell for a two-cell stack were compared with the experimental data. Second, the effects of a single-phase and two-phase of water on the performance were evaluated in a two-cell stack. Finally, a model for a 20-cell stack was constructed and used to analyze dynamic characteristics at a start-up and at a varying load.

Table 3  
Parameters for the GDL [25]

Parameters	Value
$\varepsilon$	0.5
$D_{\text{O}_2}$	$3.03 \times 10^{-5} (\text{m}^2 \text{s}^{-1})$
$D_{\text{vapour}}$	$3.45 \times 10^{-5} (\text{m}^2 \text{s}^{-1})$
$K$	$2.55 \times 10^{-13} (\text{m}^2)$
$ dp_c/dS $	30.321 (Pa)
$s_{\text{im}}$	0.1

##### 4.1. Comparison between simulations and experiments for a two-cell stack

Using our model, we simulated a two-cell stack. The  $I$ – $V$  characteristics calculated for the stack as well as the individual cells were compared with the experimental data collected at a test station installed at Auburn University. Operating conditions were as follows where the stoichiometric ratio for the anode was 1.2 and for the cathode was 3.0. The gas pressure and supply gas temperature on both sides were 1.0 bar and 333.15 K, respectively. The relative humidity for the anode gas was 0% and for the cathode gas was 100%. The average temperature of the coolants at the exits of cells 1 and 2 were maintained at 333.15 K by controlling the coolant temperature.

Fig. 4 shows simulated and experimental results of the voltage across the stack (a) and the cells (b). The simulated and experimental stack voltages matched well, but the deviation of the simulated two cell voltages was not as large as that measured experimentally. Differences in the two cells could be caused by non-uniform characteristics of the individual cells such as reactant distributions and the properties of the GDL and the membrane. Details describing the effects of the various factors on the cell voltages are described in Park and Choe [26].

##### 4.2. Comparison of a single-phase and a two-phase model for a two-cell stack

The structure of the two-cell stack was the same as that depicted in Fig. 2 except for the addition of a separator between the two coolant channels that was used to minimize the coupled cooling effects of adjacent cells on performance. Operating conditions were as follows: the stoichiometric ratio for the anode was 1.2 and that for the cathode was 2.0. The gas pressure, supply gas temperature, and relative humidity on both sides were 1.0 bar, 333.15 K, and 100%, respectively. The average temperature of coolants at the exit of cells 1 and 2 for the single-phase model was maintained at 333.15 K by controlling the coolant inlet temperature, and the coolant flow rate was constant at  $0.003 \text{ kg s}^{-1}$ . The two-phase model used the same coolant temperature and flow rate.

Static and dynamic characteristics of a two-cell stack are illustrated in Fig. 5. Fig. 5(a) shows two major effects in that

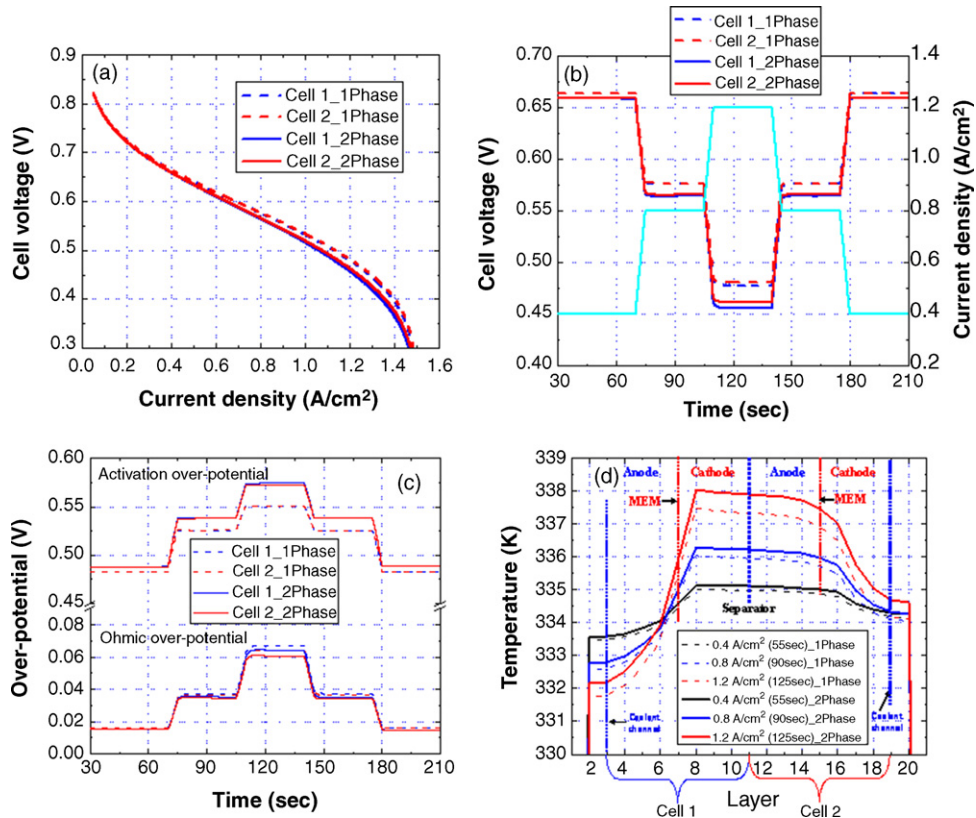


Fig. 5.  $I$ - $V$  curve and dynamic response of fuel cells during step changes in current density. (a) Calculated polarization curves of single-phase and two-phase models for a two-cell stack. (b) Variation of cell voltage during step changes in current density, (c) variation of activation and ohmic over-potentials, (d) temperature distribution in a two-cell stack.

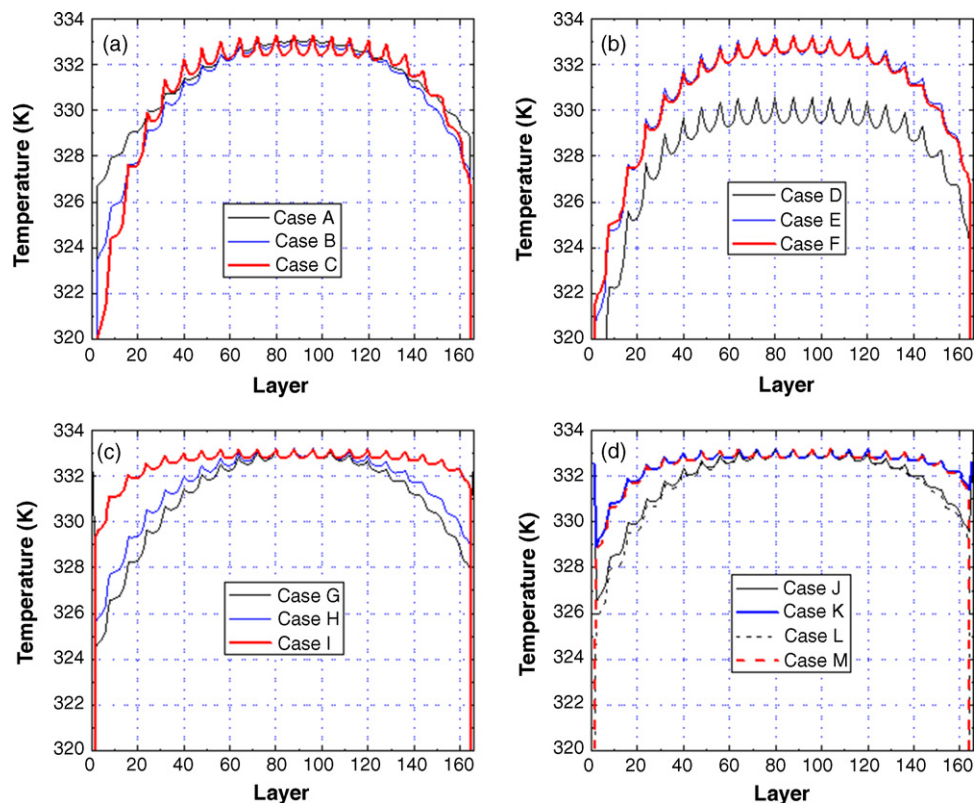


Fig. 6. Temperature distribution in the layers of a 20-cell stack for start-up in different cases.

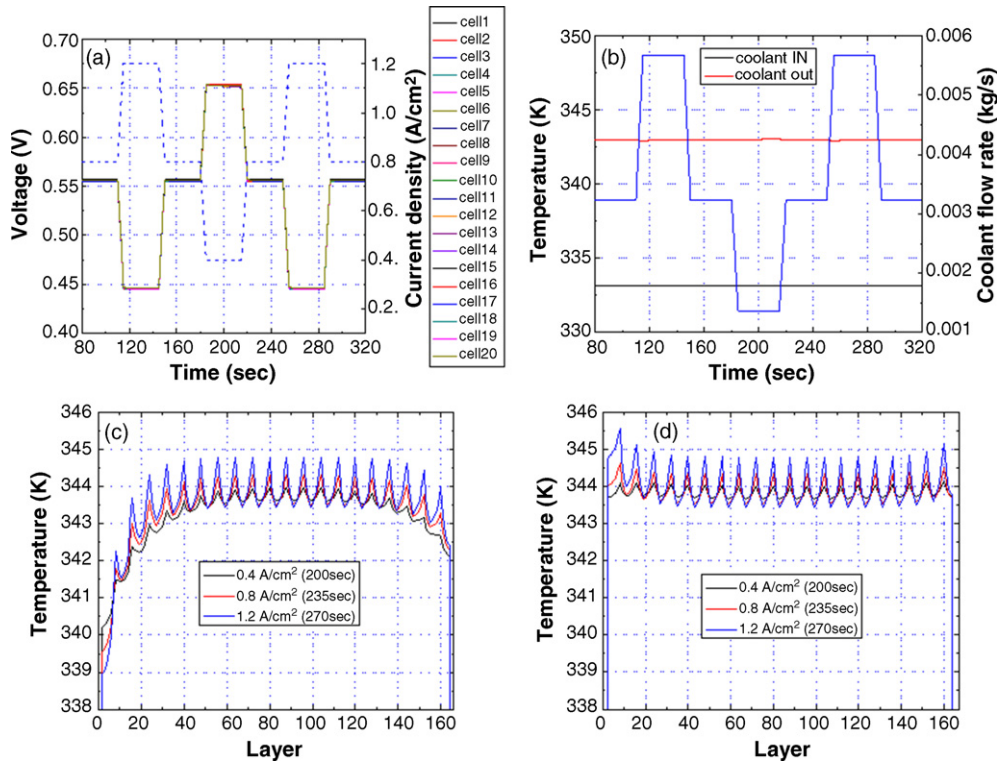


Fig. 7. The dynamic response of the cell voltage during step change in current density (a), (b) coolant flow rate and coolant temperature, (c and d) temperature distribution through the layer during step changes in the current density (0.4, 0.8 and 1.2 A cm<sup>-2</sup>).

the voltage of the two models were different from each other and that the deviation of the voltages between cells 1 and 2 was larger as the load current increased. The difference in the cell voltages between a single- and two-phase models is affected by liquid water that is otherwise neglected. As the density of the load current is higher than 0.4 A cm<sup>-2</sup>, the influence of liquid water on the performance of the cells increased and the difference between the cells was larger. As a result, the voltage drop at the two-phase model is larger than that at the single-phase model. In addition, the high voltage in cell 2 is caused by different working temperatures that depend upon the location of the

cells and the coolant channel. However, it should be noted that the liquid water did not significantly affect the limiting current density in comparison to results of other analyses because the gradient of water concentration, the pressure and temperature drop along the flow channel have not been fully considered in the modeling [6,30,31].

Fig. 5(b) shows the dynamic response of a current load profile on the cell voltages. Three amplitudes of the current density (0.4, 0.8 and 1.2 A cm<sup>-2</sup>) were applied to observe the responses. Two major phenomena were observed. First, the voltages of the cells with a two-phase model were lower than those with

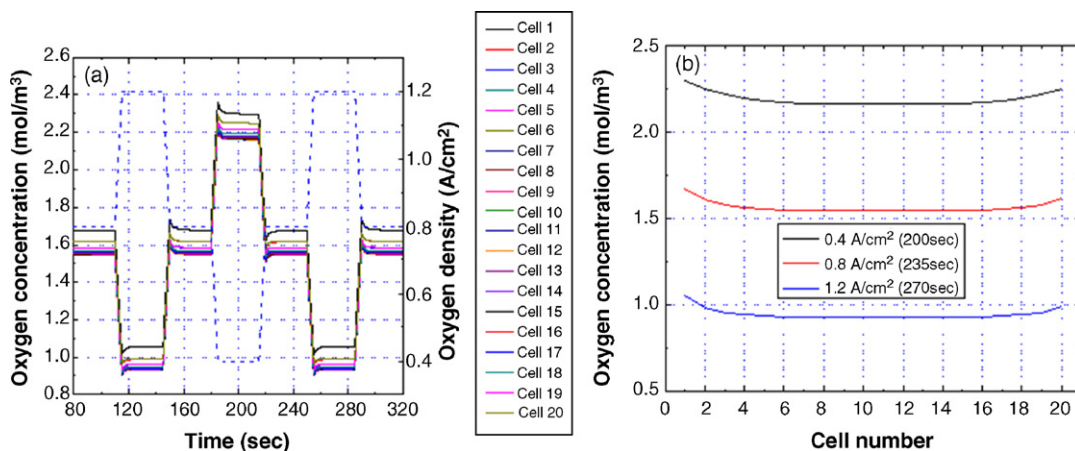


Fig. 8. The dynamic response of the oxygen concentration during step changes in current density (a), (b) oxygen concentration throughout the stack.

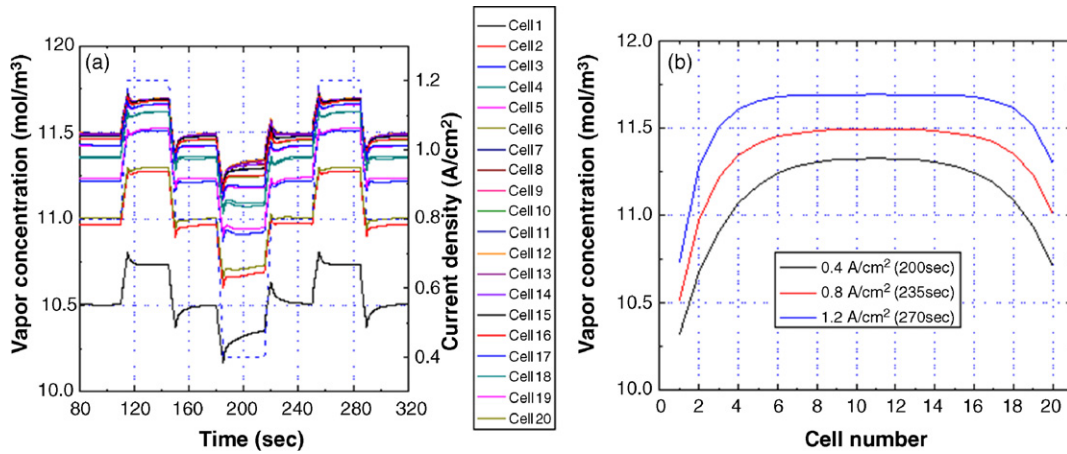


Fig. 9. The dynamic response of the vapor concentration during step changes in current density (a), (b) vapor concentration throughout the stack.

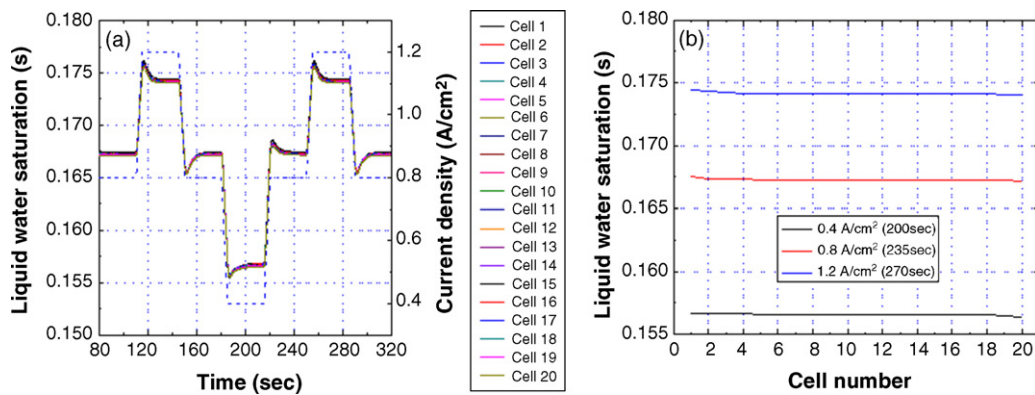


Fig. 10. The dynamic step response of liquid water saturation at a nearby cathode catalyst layer during step changes of current density (a), (b) liquid water saturation distribution throughout the stack.

a single-phase model. Second, the higher the current density the larger the voltage drop caused by the two-phase effect. Consideration of the presence of liquid water in the gas diffusion layer changes the activation and ohmic over-potential shown in Fig. 5(c). The activation over-potential is influenced by the liquid water and independent of the location of the cells. As the liquid water in the gas diffusion layer increased, the diffusivity of oxygen was reduced and its concentration

was reduced. Consequently, the activation over-potentials of the cells became higher and the voltages of the cells became lower.

On the other hand, ohmic over-potentials are dependent on the location of the cells and are asymmetrical, and also affected by temperature in the cell. Fig. 5(d) shows a temperature distribution in the stack at the given profile of current density. When liquid water was considered, the over-potentials in the cells were

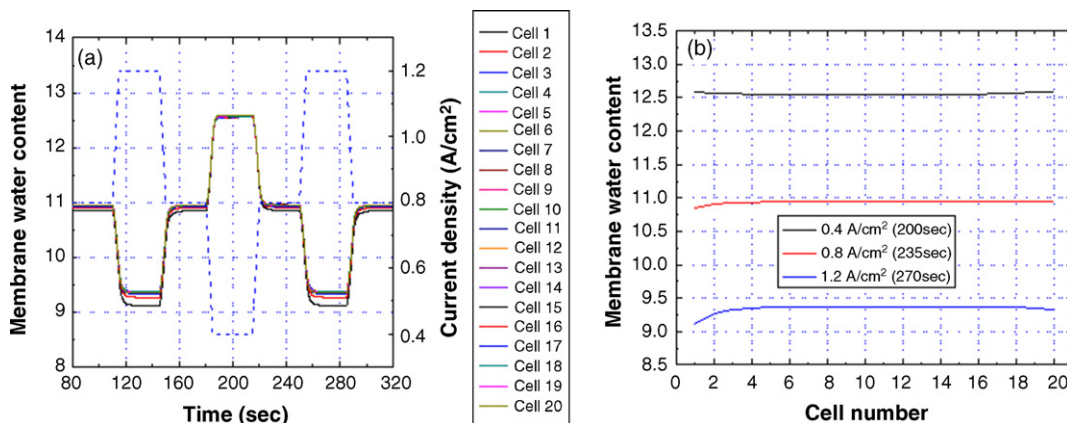


Fig. 11. The dynamic response of the membrane water content during step changes in current density (a), (b) membrane water content throughout the stack.

higher than those in a single-phase model and subsequently the associated heat produced was more than that observed in a single-phase model. As a result, the working temperature in the cells became higher. In addition, the geometrical distribution of the heat sources in the stack was asymmetrical. Accordingly, heat conductivity from the heat sources to the coolants was not identical, which caused an asymmetrical temperature profile in that the temperature in cell 1 was higher than that in cell 2. The ohmic over-potential was affected by the temperature and water content in the membrane, and the temperature in the membrane of cell 2 was higher than that of cell 1. In addition, the cathode gas channel temperature of cell 2 was lower than that of cell 1, and the saturation vapor pressure was also lower, which augments the RH in cell 2 and water content. Consequently, the ohmic over-potential in cell 2 became lower than that in cell 1 and determined the deviation of the amplitude of the two cell voltages.

#### 4.3. Analysis of a 20-cell stack

Start-up, normal operation, and shutdown are processes needed for operation of a stack. We investigated the behavior of a 20-cell stack at a start-up and under normal operations using the proposed model.

##### 4.3.1. Start-up

Dynamic behavior of a start-up is particularly important to ensure a short start-up time along with a high efficiency. In general, the optimal operating temperature of a PEM fuel cell is from 333.15 to 353.15 K. This facilitates relatively high chemical reactions and allows the water produced to be easily removed, while maintaining the membrane at a proper operating temperature.

A cold stack after a shutdown can be deployed in different environments, as example, under a freezing temperature where moisture residing inside the stack should have formed ices or, alternatively, above the freezing temperature. Start-up behavior of a frozen stack used for mobile applications has been theoretically and experimentally investigated [16,20,32–34]. However, the start-up behavior of a stack above the freezing temperature has not been fully investigated. In fact, a low working temperature of a stack decreases its performance because of increased kinetic losses, and ohmic and reactant transport losses caused by a high rate of condensation. Thus, it is necessary to elevate the working temperature of a stack as quickly as possible to meet the demands of the required load power.

Different start-up strategies were compared in the studies described below. The optimal working temperature of the stack was assumed to be 333.15 K. Operating conditions were as follows: the stoichiometric ratio for the anode was 1.2 and that for the cathode was 2.0. The pressure, temperature and relative humidity of hydrogen on the anode side were set to 1.2 bar, 298.15 K and 0%, respectively, while those on the cathode side were 1.0 bar, 338.15 K and 100%. The unconsumed hydrogen was recirculated to the stack. Table 4 summarizes the heat-up time of a stack using different start-up strategies. The initial temperature of the stack was assumed to be 298.15 K.

In cases A, B and C, we assumed that current density was applied as a step. The heat-up time became shorter as the amplitude of the current applied became higher. However, selection of a current density should be carefully determined after consideration of the maximum allowed temperature and the associated thermal energy for the membrane and the catalyst. In cases D, E and F, the current density was increased with a different slope, from 0.2 to 1.0 A cm<sup>-2</sup>, where no coolant was supplied. When the current was increased within 30 s, the stack had not achieved the set working temperature. It took a minimum of 40 s for the stack to achieve the working temperature. Case G, assumed that the initial temperature of the end plate was 333.15 K. As compared with case B, the heat-up time in case G was not reduced by heating the end plates. Cases H and I assumed that the initial temperature of the end plate was 298.15 K and that of the coolant was 298.15 K with a constant flow rate of 0.0005 and 0.003 kg s<sup>-1</sup> that excluded any heat exchanger. Compared with case B, the heat-up time was increased because of the heat transfer from the stack to the coolant when the temperature of the coolant was the same as that of the stack at the initial state. Cases J and K assumed different coolant flow rates of 0.0005 and 0.003 kg s<sup>-1</sup>, respectively, where the temperature of the coolants was controlled at 333.15 K. Case J allowed for a 15.7 s reduction of the start-up time relative to case G. In addition, in case K the heat-up time was reduced by 35.8 s. Cases L and M showed start-up times similar to those of cases J and K regardless of the temperature of the end plates.

Temperature distributions in the 20-cell stack under various start-up conditions are summarized in Table 4 and shown in Fig. 6(a–d). The graphs for the temperature profiles were captured after the heat-up time. Ohmic losses by the membrane resistances and the heat released by the chemical reaction in the catalysts caused the highest peaks among others with an asymmetrical temperature distribution throughout the cell.

When the amplitude of applied current was 0.2, 0.4, 0.8 A cm<sup>-2</sup> (cases A, B and C), the temperature difference ( $\Delta T$ ) between the layer with a maximum value (333.15 K) and the catalyst temperature of cell 1 became 5.26, 7.42, and 8.76 K, respectively. The deviation ( $\Delta T$ ) shown in Fig. 6(a) was larger with increasing current. Because of the high current density, a large amount of heat was produced in a short time and the temperature rose rapidly through the cells, particularly in the middle cell.

When the coolant inlet temperature was 333.15 K (cases L and M), the temperature difference  $\Delta T$  was reduced 5.25 and 2.56 K, respectively. The asymmetric stack temperature distribution was minimized when supplying coolants with elevated temperature.

#### 4.4. Transient response

In the following section, transient behaviors of a 20-cell stack were investigated. Operating conditions were the same as those in Section 4.3. The coolant inlet temperature was kept at 333.15 K as shown in Fig. 7(b). The average temperature of the coolant channel outlet temperature was controlled at 343.15 K

Table 4  
Heat-up time at various operating conditions

Case	Constant current density ( $\text{A cm}^{-2}$ )	Time for increasing current density 0.2–1.0 $\text{A cm}^{-2}$ (s)	End plate initial temperature (K)	Coolant flow rate for each coolant channel ( $\text{kg s}^{-1}$ )	Coolant inlet temperature (K)	Temperature difference ( $\Delta T$ )	Heat-up time (s)
A	0.2	–	298.15	No-coolant	–	5.26	125.9
B	0.4	–	298.15	No-coolant	–	7.42	54.0
C	0.8	–	298.15	No-coolant	–	8.76	21.3
D	–	30	298.15	No-coolant	–	–	–
E	–	60	298.15	No-coolant	–	8.41	42.9
F	–	90	298.15	No-coolant	–	8.14	50.6
G	0.4	–	333.15	No-coolant	–	6.58	53.9
H	0.4	–	333.15	0.0005	298.15 (circulation)	5.44	55.2
I	0.4	–	333.15	0.003	298.15 (circulation)	2.05	56.7
J	0.4	–	333.15	0.0005	333.15	4.69	38.2
K	0.4	–	333.15	0.003	333.15	2.35	18.1
L	0.4	–	298.15	0.0005	333.15	5.25	38.2
M	0.4	–	298.15	0.003	333.15	2.56	18.1

by the coolant inlet flow rate as the current density varied. The coolant flow rate refers to that rate of coolant supplied to a coolant channel.

When a step current was applied as a load, the voltage of the cells varied. As seen in Fig. 7(a), no significant difference between the individual cells was observed. In the operation of a real stack, there are differences in the  $I$ - $V$  characteristic of the individual cells influenced by inherent properties of the components as well as the design parameters of the flow patterns [31] that are not considered in the proposed model. Fig. 7(c) shows the stack temperature distribution at  $0.4 \text{ A cm}^{-2}$  (200 s),  $0.8 \text{ A cm}^{-2}$  (235 s), and  $1.2 \text{ A cm}^{-2}$  (270 s). We find that the higher the current density, the higher the amplitude of the peak temperature. The maximum temperature was 1.5–2 K higher than the average temperature of the coolant outlet at a current density of  $1.2 \text{ A cm}^{-2}$ . In addition, the temperature in the catalyst of cell 1 was lower than that in cell 20 because of high heat conductivity to the coolant channels. The four cells from the anode and cathode end plate showed a temperature gradient, while the rest of the cells exhibited relatively uniform temperature distributions. When the current density increased, the temperature of the anode coolant channel in cell 1 was reversed because of increased coolant flow rates and a high gradient. However, the difference of 1.5–2 K in the cathode catalysts did not affect the cell voltages. Stack and system design should be optimized with caution to ensure a uniform temperature distribution in the stack. Depending upon the operating conditions, the stack can be locally clogged by condensed liquid water when the temperature in the region suddenly drops.

Fig. 7(d) shows the temperature distribution of the stack when the coolant flow rate at the anode side of cell 1 and cathode side of cell 20 was reduced by 1/10 of the operating condition shown in Fig. 7(c). The reverse effect in the anode coolant channel was not observed and the stack temperature was uniformly distributed in comparison to Fig. 7(c). Different coolant flow rates at the

endplates can be implemented by proper design of the number and dimensions of coolant channels.

Fig. 8(a) shows the dynamic response of the oxygen concentration at a nearby cathode catalyst layer under the same condition as shown in Fig. 7(a–c). In general, more oxygen was consumed as the load current increased and the concentration became lower. In addition, the temperature influenced the concentrations of oxygen in the cell. Fig. 8(b) shows the oxygen concentration at a nearby cathode catalyst layer of the cells. The concentration in the end cells was higher than that in the other cells because of the temperature drop in the cathode gas channel that decreased the saturation pressure and increased the condensation. Subsequently, the partial pressure of water vapor decreased and the partial pressure of oxygen increased.

Fig. 9(a) shows the dynamic response of the vapor concentration at a nearby cathode catalyst layer. In general, more vapors were generated as the load current increased and the oxygen concentration became lower. Fig. 9(b) shows the vapor concentration at a nearby cathode catalyst layer of the cells. The concentration in the end cells was lower than that in the other cells because of the influence of the temperature distributions.

Fig. 10(a) shows the dynamic response of liquid water at a nearby cathode catalyst layer to step changes in the current density. The liquid water saturation on the cathode catalyst layer followed the load profile. As the load current increased, more water was produced in the catalyst. Fig. 10(b) shows the liquid water saturation at a nearby cathode catalyst layer of the cells. The liquid water saturation in the end cells was higher than that in the other cells because of the temperature distributions.

Fig. 11(a) shows the dynamic step response of a current density on the membrane water content, while Fig. 11(b) shows the membrane water content of the cells. As the load current increased, the membrane water content decreased because of the high water uptakes from the anode to the cathode side.

## 5. Conclusions

We focused on the development of a dynamic model for a 20-cell stack that considered temperature and two-phase effects in the GDL.

The major contributions of this work are summarized as follows:

- Voltage differences between a single-phase model and two-phase model were predominantly affected by activation over-potentials caused by changes of oxygen concentration, while the voltage differences between cells 1 and 2 were caused by temperature gradients in each layer and subsequent ohmic over-potentials. However, the liquid water did not significantly affect the limiting current density when compared with the results of other analyses because the gradient of water concentration, the pressure and temperature drop along the flow channel were not fully considered in the present modeling.
- Various strategies for a start-up of a 20-cell fuel cell stack were analyzed. In general, the higher the current density and the more the coolant flow rate and temperature were increased, the shorter the heat-up time. However, the initial temperature of the end plate did not play a significant role in reducing the heat-up time. The asymmetric distribution of the voltage was minimized by supplying the coolant, and maximized as the temperature of the coolant became higher.
- Upon operation of a 20-cell stack, the four cells from each end showed a temperature gradient, while the rest of the cells maintained a relatively uniform temperature distribution, oxygen concentration, vapor concentration, liquid water saturation, and membrane water content.
- Asymmetric distribution of temperature was balanced by reduction of the coolant flow rate at both end cells, which provided a better voltage distribution at dynamic loads.

## References

- [1] S.D. Knights, K.M. Colbow, J. St-Pierre, D.P. Wilkinson, *J. Power Sources* 127 (2004) 127–134.
- [2] J. Davey, D. Wood, F. Garzon, M. Inbody, D. Guidry, PEM fuel cell durability, DOE Hydrogen Program Review, 2005.
- [3] C.W.B. Bezerra, L. Zhang, H. Liu, K. Lee, A.L.B. Marques, E.P. Marques, H. Wang, J. Zhang, *J. Power Sources* 173 (2007) 891–908.
- [4] P.J. Ferreira, G.J. la O, Y. Shao-Horn, D. Morgan, R. Makharia, S. Kocha, H.A. Gasteiger, *J. Electrochem. Soc.* 152 (11) (2005) A2256–A2271.
- [5] U. Pasaogullari, P.P. Mukherjee, C.Y. Wang, K.S. Chen, *J. Electrochem. Soc.* 154 (8) (2007) B823–B834.
- [6] H. Meng, C.Y. Wang, *J. Electrochem. Soc.* 152 (9) (2005) A1733–A1741.
- [7] T. Berning, N. Djilali, *J. Power Sources* 124 (2003) 440–452.
- [8] D. Natarajan, T.V. Nguyen, *J. Power Sources* 115 (2003) 66–80.
- [9] S. Dutta, S. Shimpalee, J.W. Van Zee, *Int. J. Heat Mass Transfer* 44 (2001) 2024–2029.
- [10] T.E. Springer, T.A. Zawodzinski, S. Gottesfeld, *J. Electrochem. Soc.* 138 (8) (1991) 2334–2341.
- [11] T.V. Nguyen, R.E. White, *J. Electrochem. Soc.* 140 (8) (1993) 2178–2186.
- [12] J.C. Amphlett, R.M. Baumert, R.F. Mann, B.A. Peppley, P.R. Roberge, *J. Electrochem. Soc.* 142 (1995) 1–8.
- [13] J.T. Pukrushpan, H. Peng, A.G. Stefanopoulou, ASME International Mechanical Engineering Congress & Exposition, IMECE2002-DSC-32051, 2002.
- [14] B.M. Eaton, Master Thesis, Virginia Technology, 2001.
- [15] P.R. Pathapati, X. Xue, J. Tang, *Renew. Energy* 30 (2005) 1–22.
- [16] M. Khandelwal, S.H. Lee, M.M. Mench, *J. Power Sources* 172 (2007) 816–830.
- [17] J.C. Amphlett, R.F. Mann, B.A. Peppley, P.R. Roberge, A. Rodrigues, *J. Power Sources* 61 (1996) 183–188.
- [18] M. Wöhr, K. Bolwin, W. Schnurnberger, M. Fischer, W. Neubrand, G. Eigenberger, *Int. J. Hydrogen Energy* 23 (3) (1998) 213–218.
- [19] B. Wetton, K. Promislow, A. Caglar, Proceeding of the Second International Conference on Fuel Cell Science Engineering and Technology, 2004.
- [20] M. Sundaresan, R.M. Moore, *J. Power Sources* 145 (2005) 534–545.
- [21] Y. Shan, S.Y. Choe, *J. Power Sources* 145 (2005) 30–39.
- [22] Y. Shan, S.Y. Choe, *J. Power Sources* 158 (2006) 274–286.
- [23] D.A. McKay, W.T. Ott, A.G. Stefanopoulou, ASME International Mechanical Engineering Congress & Exposition, No. IMECE2005-81484, 2005.
- [24] A.J. del Real, A. Arce, C. Bordons, *J. Power Sources* 173 (2007) 310–324.
- [25] J.H. Nam, M. Kaviany, *Int. J. Heat Mass Transfer* 46 (2003) 4595–4611.
- [26] S.K. Park, S.Y. Choe, *J. Fuel Cell Sci. Technol.* (2008), in press.
- [27] M.J. Lampinen, M. Fomino, *J. Electrochem. Soc.* 140 (12) (1993) 3537–3546.
- [28] Z.H. Mo, X.J. Zhn, L.Y. Wei, G.Y. Cao, *Int. J. Energy Res.* 30 (2006) 585–597.
- [29] J.M. Corrêa, F.A. Farret, L.N. Canha, M.G. Simões, *IEEE Trans. Ind. Electron.* 51 (5) (2004) 1103–1112.
- [30] P.A.C. Chang, J. St-Pierre, J. Stumper, B. Wetton, *J. Power Sources* 162 (2006) 340–355.
- [31] P. Rodatz, F. Büchi, C. Onder, L. Guzzella, *J. Power Sources* 162 (2004) 208–217.
- [32] Q. Yan, H. Toghiani, Y.W. Lee, K. Liang, H. Causey, *J. Power Sources* 160 (2006) 1242–1250.
- [33] R.K. Ahluwalia, X. Wang, *J. Power Sources* 162 (2006) 502–512.
- [34] E.L. Thompson, J. Jorne, H.A. Gasteiger, *J. Electrochem. Soc.* 154 (8) (2007) B783–B792.